

Dooroo Kim

Woodruff School of Mechanical Engineering,
Georgia Institute of Technology,
Atlanta, GA 30332

Laura Strickland

Woodruff School of Mechanical Engineering,
Georgia Institute of Technology,
Atlanta, GA 30332

Matthew Gross

Guggenheim School of Aerospace Engineering,
Georgia Institute of Technology,
Atlanta, GA 30332

Jonathan Rogers

Woodruff School of Mechanical Engineering,
Georgia Institute of Technology,
Atlanta, GA 30332
e-mail: jonathan.rogers@me.gatech.edu

Mark Costello

Guggenheim School of Aerospace Engineering,
Georgia Institute of Technology,
Atlanta, GA 30332

Frank Fresconi

Guided Weapons, Weapons and
Materials Research Directorate,
U.S. Army Research Laboratory,
Aberdeen Proving Ground,
Aberdeen, MD 21005

Ilmars Celmins

Weapons and Materials Research Directorate,
U.S. Army Research Laboratory,
Aberdeen Proving Ground,
Aberdeen, MD 21005

Actuator Design and Flight Testing of an Active Microspoiler-Equipped Projectile

Actively controlled gun-launched projectiles require a means of modifying the projectile flight trajectory. While numerous potential mechanisms exist, microspoiler devices have been shown to be a promising control actuator for fin-stabilized projectiles in supersonic flight. These devices induce a trim force and moment generated by the boundary layer–shock interaction between the projectile body, rear stabilizing fins, and microspoilers. Previous investigations of microspoiler mechanisms have established estimates of baseline control authority, but experimental results have been restricted to cases in which the mechanism was statically deployed. This paper details the design and flight testing of a projectile equipped with a set of active microspoilers. A mechanical actuator is proposed that exhibits unique advantages in terms of robustness, simplicity, gun-launch survivability, and bandwidth compared to other projectile actuator mechanisms considered to date. A set of integrated test projectiles is constructed using this actuator design, and flight experiments are performed in which the microspoilers are oscillated near the projectile roll frequency. Data obtained from these flight tests are used in parameter estimation studies to experimentally characterize the aerodynamic effects of actively oscillating microspoilers. These predictions compare favorably with estimates obtained from computational fluid dynamics (CFD). Overall, the results presented here demonstrate that actively controlled microspoilers can generate reasonably high levels of lateral acceleration suitable for trajectory modification in many smart-weapons applications. [DOI: 10.1115/1.4036808]

1 Introduction

Gun-launched guided projectiles are an emerging class of weapons that integrate control mechanisms and microelectronics within a suitable flight body. A critical component of guided projectiles is the control actuator mechanism, which generates the needed control forces and moments for trajectory modification. In the missile community, the standard control effector is the variable-incidence fin, which has been employed on missiles of multiple scales dating back to the 1940s [1]. However, the use of variable-incidence fins for gun-launched munitions poses unique challenges due to several factors including in-barrel survivability, drag penalties during fin deployment, and complexity of the actuator mechanism. As a result, a variety of novel control-effector concepts designed specifically for gun-launched precision munitions have been proposed. These include aerodynamic mechanisms such as canards [2,3], ram air deflectors [4,5], and

moveable noses [6,7], which rely on aerodynamic effects to provide control. Others, such as gas or explosive thrusters [8,9], rely on on-board thrust mechanisms. A third class of actuator designs, inertial load mechanisms, change fundamental mass properties of the projectile, leading to aerodynamically induced control forces [10,11]. One challenge faced by nearly all of these mechanisms is lack of control authority. For example, in the case of canards, space constraints limit the surface area that may be exposed to the flow. Likewise, for internal moving-mass actuation [12], narrow projectile geometries limit throw of the internal mass, providing only mediocre control authority in most cases.

This paper considers one type of aerodynamic mechanism, termed microspoilers, which have been shown to be a promising control mechanism in previous investigations [13–15]. Microspoilers are small flow-effector mechanisms that extend orthogonally to the projectile body and are typically located between the rear stabilizing fin sets of a finned projectile. The boundary layer–shock interaction between the projectile body, the microspoilers, and the rear fin set acts to produce rather large control forces and moments at relatively low drag penalty. Microspoilers were originally introduced as a candidate control mechanism by Dykes et al. [13], who predicted the control authority induced by the mechanism using aerodynamic coefficients obtained through computational fluid dynamics (CFD). In a subsequent experimental study, Scheuermann et al. [14] constructed a small-scale finned

Contributed by the Dynamic Systems Division of ASME for publication in the JOURNAL OF DYNAMIC SYSTEMS, MEASUREMENT, AND CONTROL. Manuscript received October 27, 2016; final manuscript received April 28, 2017; published online July 10, 2017. Assoc. Editor: Soo Jeon.

The United States Government retains, and by accepting the article for publication, the publisher acknowledges that the United States Government retains, a nonexclusive, paid-up, irrevocable, worldwide license to publish or reproduce the published form of this work, or allow others to do so, for United States Government purposes.

projectile with statically deployed microspoilers and obtained spark range measurements that were used to estimate aerodynamic coefficients. Most recently, Leonard et al. [15] investigated possible geometric arrangements of microspoilers on the projectile surface and obtained an optimal configuration that maximizes control authority. In a separate set of investigations, Massey et al. [16–18] considered a control mechanism called “pin fins,” which are similar to microspoilers except they are larger (on the order of one-third the fin height) and protrude beyond the boundary layer. Both computational and experimental analysis showed that significant force multiplication can be generated by modifying the boundary layer–shock interaction of the projectile fin and body, leading to large and controllable aerodynamic load perturbations.

In addition to deficiencies in control authority, another challenge typically encountered by smart-weapons designers is the mechanical design of the actuator itself. Viable mechanical actuator designs must be low-cost, capable of actuating at frequencies near the projectile spin rate, and robust to large acceleration loads at launch which can reach well above 50,000 g. Numerous authors have proposed mechanical actuator concepts that satisfy at least some of these design goals. A selected set of prior work is described here for illustrative purposes and is not meant to be an exhaustive list. Celmins [19] proposed an actuator design using a linear solenoid combined with a spring tab, showing favorable performance at an actuator frequency of 60 Hz for a low number of cycles. Fresconi et al. [20] proposed an actuator that uses a linear voice coil to control a pair of variable-incidence canards. This single-degree-of-freedom design was experimentally verified to survive loads in excess of 20,000 g. More recently, Kang et al. [21] reported an actuator concept for a two-state projectile control mechanism comprised of a bistable plate which is actuated via a piezo-electric device. Another novel concept proposed by Celmins et al. [22] for man-portable munitions uses a set of motors at the rear of the projectile to move a static airfoil into and out of the oncoming airflow. A final control actuator particularly relevant to this paper was proposed by Massey and Silton [18] for pin-fin mechanisms. This device is purely passive and involves a spring-mass system which yields oscillatory motion of the fins into and out of the projectile body. While robust to very large launch loads, the mechanism is meant only for aerodynamic characterization and does not allow for active control of the fin deployment cycle during performance of guidance maneuvers. In spite of the extensive prior work performed in this area, there is a continuing need for low-cost, robust actuator concepts that can survive gun launch and that can be tailored to specific control mechanisms such as canards or microspoilers that undergo periodic excitation at the projectile roll rate.

In light of this prior work, the contributions of this paper are twofold. First, a novel rotary actuator concept is proposed for periodic excitation of a projectile control mechanism at typical spin rates of fin-stabilized projectiles. This actuator exhibits a favorable nonsinusoidal deployment profile and is shown to survive acceleration loads in excess of 16,000 g. Flight experiments confirmed gun-survivability of both the actuator mechanism itself as well as supporting components such as batteries and motors. The second contribution of this paper lies in experimental verification of the ability of microspoilers to produce reasonable lateral acceleration when deployed in an oscillatory fashion at a frequency near the projectile spin rate. Note that, other than the limited pin-fin experiments documented in Ref. [16], this represents the first experimental work to date verifying the control efficacy of microspoilers as they undergo active oscillation (the work in Ref. [14] studied statically deployed spoilers only). This is particularly important since active control mechanisms on spinning projectiles must provide actuation in a constant maneuver direction and thus must be activated in an oscillatory fashion at the projectile spin rate.

The paper proceeds as follows. First, the actuator concept is described in detail, and limited simulation results are provided to estimate control authority for an example fin-stabilized round.

The design of an integrated projectile is then presented. Experimental results are provided for a series of spark-range flight experiments using a set of prototype active-microspoiler projectiles. A final section describes the parameter estimation process using the spark-range data in which aerodynamic coefficients are extracted from experimental measurements. These coefficients are used to generate a new set of simulation results that confirm the ability of the microspoiler devices to generate substantial control authority when undergoing active oscillation.

2 Actuator Design

This section provides a detailed description of the proposed mechanical actuator design, as well as integration of the mechanism into an actively controlled projectile. The section begins with a discussion of the optimized microspoiler geometry used throughout this paper, as well as control authority estimates derived from CFD predictions. Actuator design is then described in detail, including discussion of several candidate actuator concepts and the down-selection process. Finally, a fully integrated projectile design is offered for the purposes of flight testing and aerodynamic characterization.

2.1 Microspoiler Actuation Concept. The microspoiler mechanism is comprised of a set of small protrusions which can extend from, and retract into, the projectile body. As shown in Fig. 1, these microspoilers are located between the rear stabilizing fins and oriented orthogonally to the projectile body. When the spoilers are extended in supersonic flight, the shock waves induced by the microspoilers interact with the stabilizing fins and projectile body, creating an aerodynamic force and moment perturbation. By extending and retracting the microspoilers in conjunction with the projectile roll angle, a control moment can be generated in a desired inertial direction so as to alter the projectile trajectory. It is important to note that the microspoiler surfaces considered here are relatively small devices designed to remain largely within the boundary layer at full extension—this is necessary in order to avoid large drag penalties at high Mach numbers. Although not shown in Fig. 1, multiple sets of spoilers may be located around the projectile between each fin set and actuated independently for maximum control authority [13].

Microspoiler control effectiveness is quantified by an induced axial force perturbation, normal force perturbation, and pitching moment perturbation. To define these quantities, consider an inertial frame I and a projectile body frame B , where the body frame is obtained from the I frame by rotating about the standard aerospace Euler angle rotation sequence. In this paper, the projectile roll, pitch, and yaw Euler angles are denoted by ϕ , θ , and ψ , respectively. The aerodynamic forces generated by the microspoilers are modeled as trim forces acting at the projectile mass center and include both axial and normal force components according to

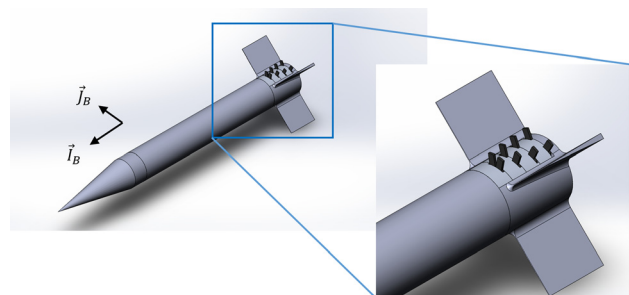


Fig. 1 Microspoiler mechanism on-board a fin-stabilized projectile

$$\begin{Bmatrix} X_{MS} \\ Y_{MS} \\ Z_{MS} \end{Bmatrix} = \begin{Bmatrix} \delta_A(s) \\ \delta_{NY}(s) \\ \delta_{NZ}(s) \end{Bmatrix} \quad (1)$$

where X_{MS} is the axial force perturbation along the \mathbf{I}_B axis, Y_{MS} and Z_{MS} are the normal force perturbations along the \mathbf{J}_B and \mathbf{K}_B axes, respectively, and δ_A , δ_{NY} , and δ_{NZ} are the induced trim forces at full spoiler extension. In Eq. (1), a variable $0 \leq s \leq 1$ is introduced to represent the degree to which the spoiler is extended, with $s=0$ representing the fully retracted position and $s=1$ representing the fully extended position. In the current work, the force dependency on spoiler position is modeled as linear such that

$$\begin{Bmatrix} \delta_A(s) \\ \delta_{NY}(s) \\ \delta_{NZ}(s) \end{Bmatrix} = \begin{Bmatrix} \delta_A \cdot s \\ \delta_{NY} \cdot s \\ \delta_{NZ} \cdot s \end{Bmatrix} \quad (2)$$

Note that in general, a nonlinear relationship may exist between the force components and the spoiler position. However, in light of the limited aeroprediction data available in this study, a linear model is assumed and development of a more complex model is left to future work.

Similarly, the microspoiler moment perturbation is represented as a trim aerodynamic moment that, in general, can act to produce a trim roll, pitch, and/or yaw moment about the projectile mass center. The microspoiler moment is given by

$$\begin{Bmatrix} L_{MS} \\ M_{MS} \\ N_{MS} \end{Bmatrix} = \begin{Bmatrix} \delta_L \cdot s \\ \delta_M \cdot s \\ \delta_N \cdot s \end{Bmatrix} \quad (3)$$

where again a linear relationship is assumed between the trim aerodynamic moment and the spoiler extension value. In Eq. (3), δ_L , δ_M , and δ_N are the trim aerodynamic moments induced by the microspoiler mechanism at full extension ($s=1$). Note that for an arbitrary geometrical arrangement of the spoilers, all six perturbation force and moment values (δ_A , δ_{NY} , δ_{NZ} , δ_L , δ_M , δ_N) may be nonzero. In this paper, only configurations that are symmetrical about the centerline, and in which the spoilers are facing orthogonally to the projectile axis of symmetry, are considered. For this subset of configurations, δ_L and δ_N are small enough to be negligible and are, thus, set to zero. Furthermore, as shown in Fig. 1, only a single set of spoilers is considered between two aft fins, oriented so that the perturbation normal force δ_{NY} is approximately zero. Thus, the remaining nonzero force and moment perturbations produced by the spoiler geometry considered in this paper are the axial force δ_A , normal force δ_{NZ} , and pitching moment δ_M .

There are potentially numerous ways that one can geometrically configure the microspoiler devices. Possible configuration variables include the number of spoilers between a given set of fins, their geometrical arrangement, proximity to the fins, spoiler

height, spoiler depth, spoiler width, and potentially other factors such as sweep angle. A recent investigation by the authors documented in Ref. [15] used a series of CFD studies to identify a microspoiler configuration that provided an optimal tradeoff in terms of control authority, drag penalty, and mechanical complexity. A number of CFD simulations were performed in which the drag, normal force, and pitching moment generated by the mechanism were estimated and compared between configurations. The example projectile used in these configuration optimization studies was the 30 mm-diameter Army-Navy Finner (ANF) projectile. A schematic of this projectile is shown in Fig. 2. This projectile was selected because of its routine use in academic literature and its well-characterized aerodynamic properties. Likewise, in the study documented here, the 30 mm ANF projectile is selected as the example testbed for all simulation and experimental results. However, it is important to note that the results discussed here are not limited to this airframe only and can reasonably be assumed to generalize to various classes of fin-stabilized projectiles.

The optimized microspoiler configuration produced by the studies in Ref. [15] is shown in Fig. 3. In this setup, a total of eight spoilers are used, arranged in a v-formation such that the last row is near the aft end of the projectile. The height of the microspoilers in this configuration is 5 mm at full extension, uniform across all spoilers. Figure 4 shows the microspoiler force and moment perturbation values predicted by CFD as a function of angle of attack at Mach 2.5. Additional aerodynamic predictions documented in Ref. [15] indicate that the pitching moment induced by the microspoilers, which is responsible for the majority of the mechanism's control authority, scales approximately linearly with Mach number. Note that, in comparison to the four-spoiler designs used previously in Refs. [13,14], the optimized geometry obtained in Ref. [15] exhibits an impressive 80% increase in control moment with only a 39% increase in drag. This geometry is used for all simulation and experimental studies discussed in the remainder of this paper.

To demonstrate the overall control authority of this mechanism, a simulation is presented using an industry standard six degrees-of-freedom projectile dynamic model described in Ref. [23]. The 30 mm ANF projectile is fired at zero gun elevation with no gravity at a muzzle velocity of Mach 2.5. The projectile is assumed to be equipped with four sets of spoilers, one between each set of fins. The microspoilers are extended in a sinusoidal profile matched to the roll frequency with a phase angle such that maximum control is generated in the negative cross-range direction. The projectile has a mass of 0.840 kg and axial and transverse inertias of $1.02 \times 10^{-4} \text{ kg/m}^2$ and $4.56 \times 10^{-3} \text{ kg/m}^2$, respectively. Figure 5 shows cross-range travel as a function of range, where the trajectory of a baseline ANF projectile (without microspoilers) is also shown for comparison. In the controlled case, a steady-state angle of attack of approximately 2.2 deg is exhibited. Measuring the total trajectory deviation of approximately 55 m over a time of flight of about 1.2 s, this yields an average lateral acceleration of 7.8 g provided by this control mechanism.

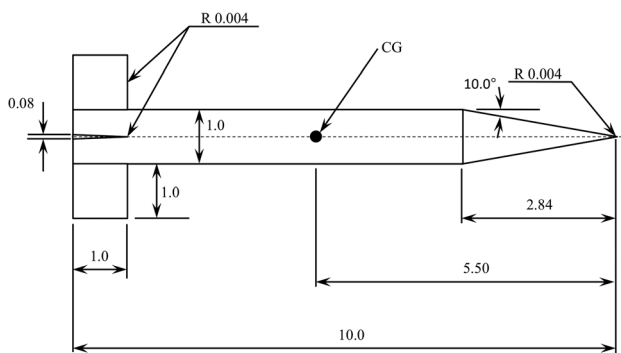


Fig. 2 Army-Navy Finner projectile. All dimensions in calibers.

2.2 Candidate Actuator Designs. Given this optimized spoiler geometry, an actuator concept was designed for use in subsequent flight experiments. As will be discussed, the purpose of these flight experiments was to gather spark range data which could then be used to experimentally characterize the forces and moments induced by the microspoilers. The overall design requirements employed during this process were determined based on an assumed muzzle velocity of Mach 2, and a relatively short time of flight of about 400 ms. This is consistent with the test parameters of the Army Research Lab's Transonic Experimental Facility (TEF) discussed in Sec. 2.3. Based on this flight profile, it was determined that the actuator needed to survive launch loads of 16,000 g and be capable of actuation at the predicted roll frequency of about 70 Hz. Furthermore, it was desired that the actuator concept exhibit minimal mechanical complexity

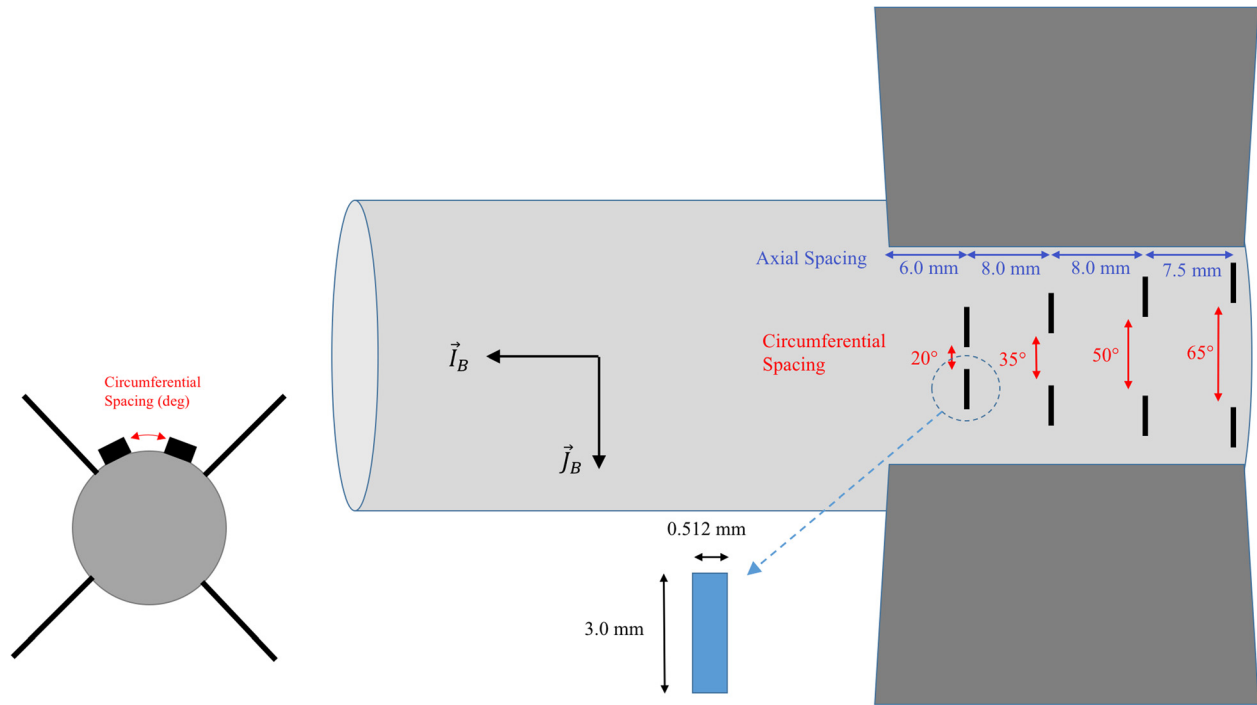


Fig. 3 Optimized microspoiler geometry identified in CFD studies [15]

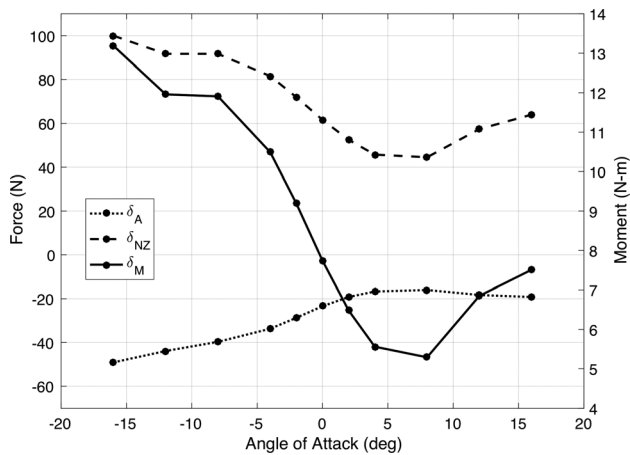


Fig. 4 Microspoiler forces and moments versus angle of attack, Mach 2.5 [15]

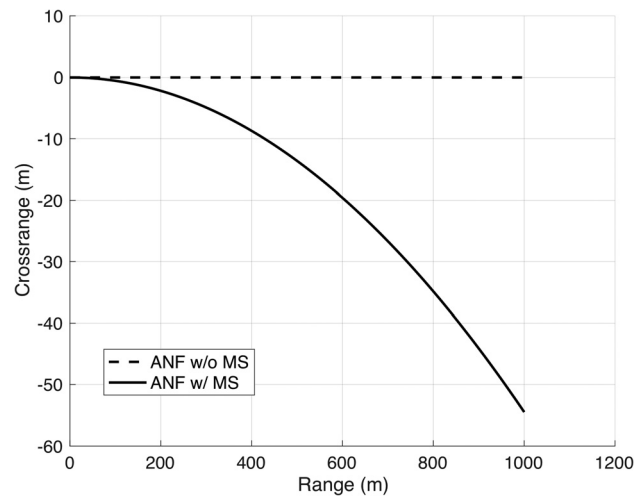


Fig. 5 Cross-range versus range for example trajectory simulation

in order to reduce design and fabrication costs as much as possible.

Two basic modes of actuation were considered—a linear solenoid approach and a rotary actuator approach. The solenoid concepts were similar to those investigated by Celmins [19] in which one or more linear solenoids are used to actuate one or more spoiler devices, possibly in conjunction with a spring tab. However, the linear solenoid designs in which eight spoilers were actuated simultaneously were deemed to be too mechanically complex. Using a single solenoid to drive all spoilers guaranteed in-phase motion of each spoiler but was mechanically complex since each pair of spoilers lies in a different vertical plane. Alternatively, the use of individual solenoids to drive each pair of spoilers was problematic due to insufficient space in which to locate four solenoids in the area available. As a secondary consideration, rotary actuators were viewed as having better robustness against the large (and somewhat uncertain) axial loads during launch and inflight. As a result of these factors, it was decided to

pursue a rotary actuator mechanism for the test projectiles designed here.

Four different rotary actuator concepts were investigated, all based to some degree on a motor-cam design. These actuator designs, depicted in Fig. 6, were a Scotch yoke Fig. 6(a), modified Scotch yoke Fig. 6(b), positive return mechanism Fig. 6(c) [24], and cam-follower mechanism Fig. 6(d). In each design, each pair of spoilers is attached to a plate embedded between spacers inside the projectile, where the plate is restricted to linear motion along the spoiler extension axis. Rotational motion of the cam forces the spoiler plates into the desired single-axis, oscillatory motion. In the Scotch yoke and modified Scotch yoke designs, the spoiler plate has a groove which rides on a pin. This pin is attached off-center to a circular plate, which is driven by a motor. The positive return mechanism is a similar concept, except that the pin is replaced by a Reuleaux triangle, which changes the actuation profile of the spoilers as a function of the motor shaft angle. Finally,

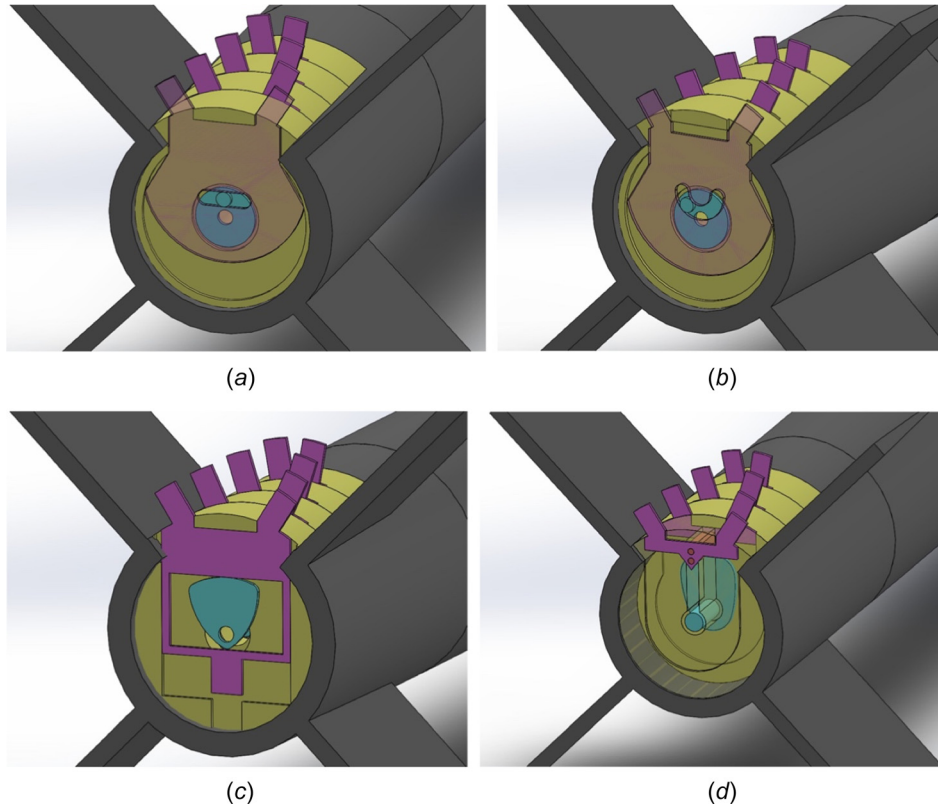


Fig. 6 Candidate rotary actuator mechanism designs: (a) scotch yoke design, (b) modified scotch yoke design, (c) positive return mechanism design, and (d) cam-follower design

the cam-follower design uses a specially shaped cam connected to the motor shaft to drive spoiler plate extension. The two forward spoiler plates and the two aft spoiler plates are connected together via a single-cam rider. In each of the designs depicted in Fig. 6, the motor which drives the rotating shaft is located forward of the fin assembly and faces rearward.

One important factor to consider with respect to the aforementioned design options is the spoiler extension profile as a function of the motor shaft angle. Because the shaft spins at the projectile roll frequency, this extension profile is equivalent to the window over the roll cycle during which the spoilers are deployed, called the activation window [13]. Theoretically, a 180 deg-square wave activation window provides maximum control authority in a given direction, although it is shown in Ref. [13] that an activation window of 110 deg provides the optimal tradeoff between control authority and drag penalty. The spoiler extension distance as a function of cam position for each of the four design concepts is shown in Fig. 7. This figure also shows a 180 deg-square wave and the 110 deg-square wave for comparison purposes. The Scotch yoke design provides the least desirable actuation profile (perfect sinusoid) compared to the other designs, as it is a poor approximation of both the 180 deg- and 110 deg-square waves. The modified Scotch yoke and positive return mechanism offer better approximations to the 110 deg- and 180 deg-square waves, respectively, providing steeper transitions between stowed and fully deployed configurations. However, the modified Scotch yoke exhibits high periodic torque loads on the motor shaft whenever the pin reaches the end of the groove. This was viewed as problematic in that it could affect the achievable rotation rate and lead to asymmetric rotation cycles. The cam-follower design provides the most control over the activation profile but offers no mechanism to retract the spoilers inside the body when the cam is not engaged. This necessitates the use of springs to retract the spoilers inside the airframe, which increases the mechanical complexity considerably. Overall, the positive return mechanism was viewed

as being the best tradeoff between the different designs in that it provides a suitable activation profile (close to the 180 deg square), constrains the spoilers throughout the rotation of the motor shaft, and yields only mildly asymmetric torque loads compared to the modified Scotch yoke.

The tradeoffs described previously are summarized in Table 1, where the root-mean-square errors of the extension profile with respect to the desired square wave profiles in Fig. 7 are provided. As shown in the table, the Scotch yoke has low mechanical complexity and no periodic torque loads but is a poor approximation to the desired trajectories. The modified Scotch yoke exhibits a better approximation to the 110 deg extension profile but exhibits large periodic torque loads. The cam-follower also exhibits a

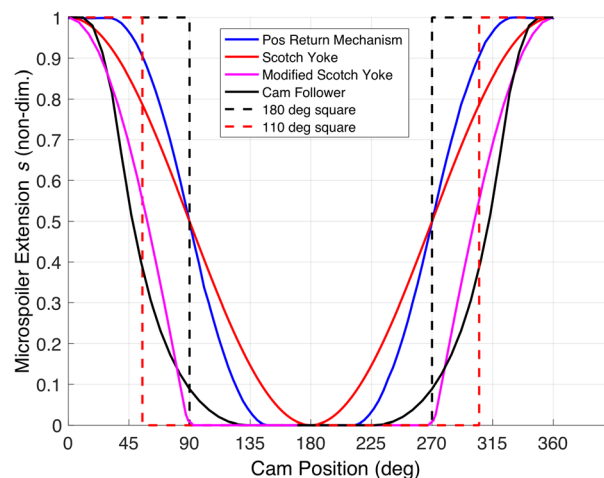


Fig. 7 Microspoiler extension versus cam angle for candidate actuator designs

Table 1 Actuator design tradeoffs (positive return mechanism selected for design)

Mechanism	Relative mechanical complexity	Root-mean-square error compared to square wave (nondim)		Periodic torque loads
		110 deg	180 deg	
Scotch yoke	Low	0.34	0.24	None
Modified scotch yoke	Low	0.23	0.51	High—due to pin reaching end of groove
Positive return mechanism	Medium—requires Reuleaux-shaped cam	0.34	0.19	Moderate—due to asymmetric torque loading on cam over rotation
Cam follower	High—requires springs to retract spoilers inside round	0.19	0.39	Moderate—due to cam engaging/disengaging follower

favorable extension profile but suffers from higher mechanical complexity. The positive return mechanism strikes an effective balance between all of these factors. Thus, this mechanism was down-selected as the actuator of choice for the subsequent flight test program.

2.3 Integrated Projectile Design. A set of test projectiles was designed and constructed for use in spark range flight experiments at the Transonic Experimental Facility (TEF) at Aberdeen Proving Ground, Aberdeen, MD. The purpose of these flight experiments was to gather experimental data to estimate microspoiler forces and moments and to verify that the microspoilers still maintained the predicted control forces and moments when they undergo dynamic oscillation at a frequency similar to the spin rate of typical fin-stabilized projectiles. As such, the tests were designed to generate enough control excitation with the spoilers so that trajectory perturbations were visible in the spark shadowgraphs and aerodynamic coefficients could be estimated. However, too much control excitation would be problematic since the projectile had to remain within the viewing windows of the spark stations (approximately $2\text{ m} \times 2\text{ m}$), and more importantly, within the confines of the spark range itself. Accordingly, the microspoiler actuation frequency was selected to be slightly different from the projectile roll frequency so that control moments were integrated out over a roll cycle and were not biased in a single direction. Simulations of the resulting flight path showed that it exhibited measurable angle-of-attack perturbations without significant cross-range deviation. Based on a series of simulation trade studies, the test projectile was designed to have a 1.25 deg fin cant, 70 Hz microspoiler actuation frequency, and a stationline CG position of 137 mm measured from the projectile base. Note that at the selected launch velocity of Mach 2.0, the projectile steady-state spin rate was predicted to be approximately 72 Hz. However, because it was launched smooth-bore with no initial spin, the projectile did not actually achieve this spin rate during its flight through the 400 m spark range.

The flight tests performed here were designed only to generate sufficient control excitation for parameter estimation and thus required only very limited electronics. The microspoiler actuator was not tied to the projectile roll angle (as it would normally be in actual maneuvering flight) and was instead operated open-loop at a constant frequency. Thus, the only electronics incorporated into the projectile was a circuit designed to activate the spoiler mechanism at gun launch. A latch activation circuit was used for this purpose [25]. The latch circuit is constructed using two MOSFET transistors and a shock switch, such that when the shock switch is activated, the motor circuit latches on (permanently). Thus, momentary closure of the shock switch during gun launch activates the motor for the remainder of the flight. The shock sensor selected for use was the SignalQuest SQ-ASE, rated to switch at 4000 g. Note that this high g-activation level was selected so that the circuit would not activate accidentally during transport. The activation circuit board was integrated so that it was directly attached to the motor, as shown in Fig. 8. This figure also shows the Maxon A-Max 110147 motor selected for use in the projectile design, as well as the latch circuit schematic. Through a series of shock table experiments of various motors, the A-Max was identified as particularly robust to acceleration loads up to 26,800 g and thus was selected for use in the experiments performed here.

The spark stations at the TEF extend approximately 200 m from the gun, meaning that at Mach 2.0, the measured trajectory occurs only over a flight time of about 250 ms. Thus, it was imperative that the microspoilers accelerate to the desired actuation frequency extremely quickly after launch. The angular velocity step response of the cam mechanism depends heavily on the voltage supplied across the motor terminals. To achieve proper angular acceleration, a custom-built 16.7 V battery pack was constructed using nine Tenergy 3.7 V lithium-polymer flatpack cells (where some cells were connected in series and some in parallel). Note that these flatpack cells were selected due to their demonstrated robustness to large shocks in previous ARL experiments [26]. Figure 9 shows a time history of the microspoiler actuator step

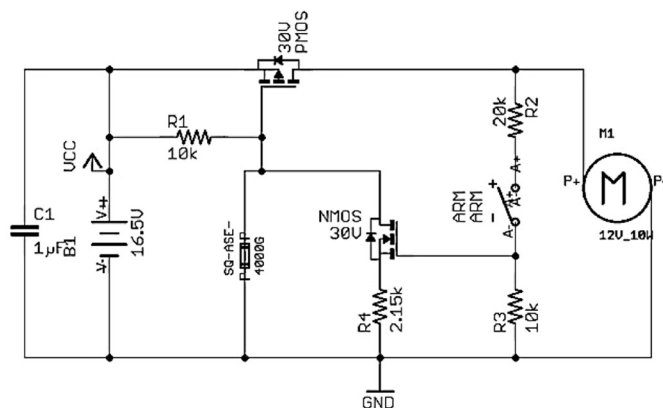
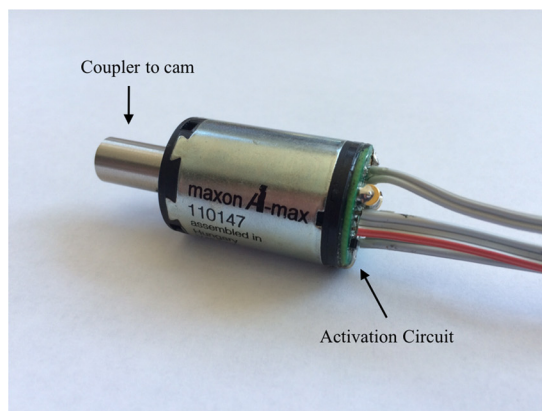


Fig. 8 Motor assembly (left) and latch circuit schematic (right) for microspoiler projectile

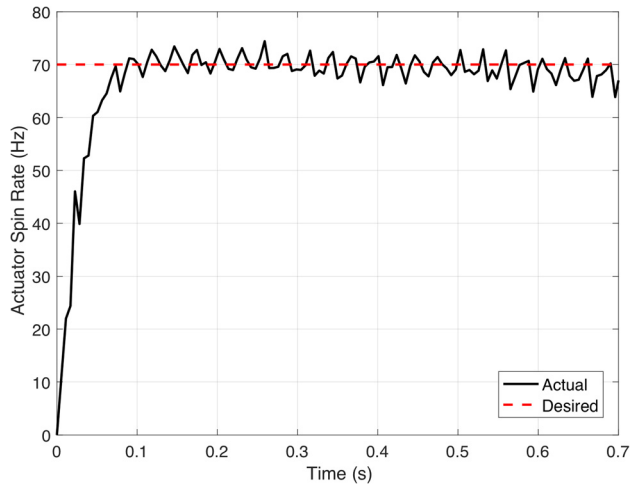


Fig. 9 Lab-characterized actuator step response

response starting from rest, obtained in laboratory experiments. In these laboratory tests, 1 lb weights were hung from each spoiler during actuation to simulate the axial aerodynamic loads on each device during flight. Note that the actuator spin rate in Fig. 9 is within 90% of its desired oscillation frequency after about 50 ms of activation. This was deemed suitable as the mechanism would be at its designed actuation frequency for 80% of the trajectory through the spark range.

It is important to note when considering Fig. 9 that the motor selection and testing process was meant only to support the spark range flight experiments described here. When designing a system for actual feedback control, the motor response time to changes in the commanded rotation phase angle must be characterized, as the phase angle is continually updated during flight and must be tracked relatively precisely by the motor. Likewise, the rotation decay rate must be characterized to determine the time delay associated with the controller temporarily pausing actuation. The actuator response shown in Fig. 9 only quantifies the initial motor rise time and does not consider the motor response to phase angle changes during rotation or the decay rate when actuation is stopped. Thus, it is meant only to support the tests performed

here. For a design meant for feedback control implementation, additional tests would need to be performed during the motor selection process.

The integrated microspoiler projectile design is shown in Figs. 10 and 11. The motor-cam assembly is installed inside the rear fin section as shown in Fig. 10. The cam is attached via a coupler mechanism to the motor, which is located just forward of the aft fin assembly and is placed against a detent in the projectile body to avoid any shock-induced motion during launch. The activation circuit is mounted directly on top of the motor, flush against the top surface. The battery pack, consisting of nine flat-pack cells, is installed forward of the motor. Each projectile was constructed from three separate pieces: a (solid) nosecone, body, and aft fin assembly. The nosecone and projectile body were machined individually from 303 stainless steel stock, while the fin assembly was machined from 7075 aluminum. Each of the three main components was designed to be individually assembled, with final integration just prior to launch. Note that all free space within the projectile body was filled with potting material (Stycast 1090) to protect against components shifting during the large launch acceleration (predicted to be upwards of 15,000 g). In addition to the projectiles themselves, sabot assemblies were designed and fabricated in order to interface with a 120 mm gun tube. Table 2 shows selected geometric and inertial characteristics of the assembled projectiles. Figure 12 shows a fully assembled aft fin section, while Fig. 13 shows a fully integrated projectile and sabot assembly. A total of 15 active microspoiler projectiles were fabricated, along with ten standard ANF projectiles (with no microspoilers) for use in comparison flights. The no-microspoiler rounds were designed to have identical dimensions, mass, and inertia to the active projectiles. Spin pins of length 1.6 cm were inserted into the base of each projectile off of the centerline axis in order to measure roll angle in the spark shadowgraphs.

3 Flight Experiments

A total of 14 flight experiments were performed in the TEF, including four baseline (no-microspoiler) projectiles and ten active projectiles. The purpose of testing the baseline projectiles was to gather experimental data with the bare airframe such that, by comparing the baseline and controlled results, the effects of the microspoilers could be isolated. In most flight experiments, the muzzle velocity was observed to be around Mach 2.0, although

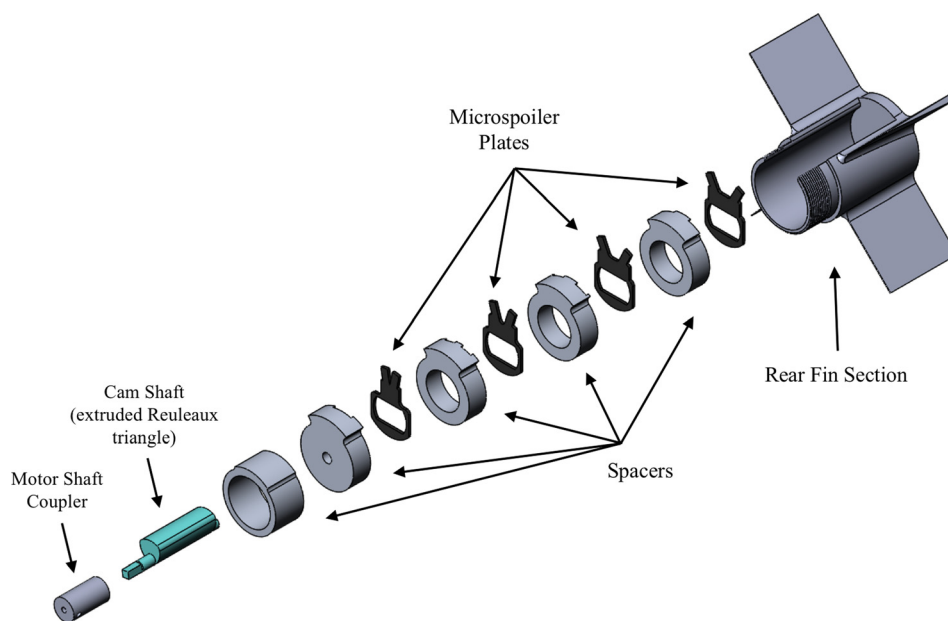


Fig. 10 Exploded view of active microspoiler assembly

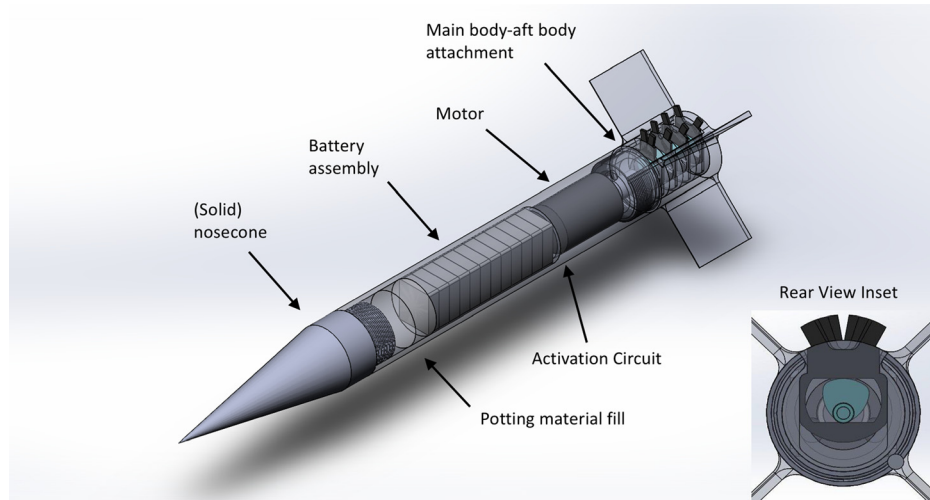


Fig. 11 Active microspoiler projectile integrated design

Table 2 Microspoiler projectile geometric and inertial parameters

Description	Value
Reference diameter, D (mm)	30.0
Mass center location (measured from base) (mm)	137
Mass (kg)	0.840
Roll inertia (kg/m^2)	1.128×10^{-4}
Pitch inertia (kg/m^2)	4.956×10^{-3}
Fin cant angle, δ (deg)	1.25
Microspoiler height at full extension (mm)	5.0



Fig. 12 Fully assembled active microspoiler assembly in aft section of projectile

several cases exhibited a higher muzzle velocity around Mach 2.5. For all active shots, an attempt was made to load the projectile with the microspoilers facing in a consistent direction. The TEF incorporates a total of 25 spark stations, arranged in groups of five separated by about 21 m. Each trajectory resulted in a set of measured position and orientation states at 20–25 different points (the number varies because spark stations sometimes fail to trigger). An example spark range shadowgraph from an active projectile flight test is shown in Fig. 14.

Prior to the flight experiments, a simulation was performed at the anticipated muzzle velocity of Mach 2.0 using the aerodynamic coefficients derived in Ref. [15]. This simulation used a square-wave actuation profile with a duty cycle approximately



Fig. 13 Fully integrated active projectile and sabot assembly

equal to that of the positive return mechanism's activation profile in Fig. 7. To replicate the test conditions as closely as possible, the projectile was launched with zero spin rate from an initial location of $x = -38.0$ m, $y = -3.48$ m, and $z = -3.25$ m, which is the measured location of the muzzle exit with respect to the first spark station. All the other initial states were set to zero, yielding a nominal trajectory free from any launch perturbations or gun-pointing errors.

Figures 15–18 show the aggregated cross-range, altitude, yaw, and pitch angle measurements, respectively, from each of the 14 experimental spark range trials which include both baseline and controlled (active) configurations. These figures also show the simulated nominal trajectory as a gray line. There are several interesting features apparent in these figures. First, in Fig. 15, several of the controlled trajectories show a slightly larger cross-range deviation compared to the baseline cases. The simulated trajectory shows relatively minimal cross-range deviation but as mentioned previously does not capture effects such as sabot separation, which may cause systematic perturbations in the experimental data. Figure 16 shows that the controlled trajectories had a consistently larger altitude reduction compared to the baseline cases, likely due to the increased drag caused by the

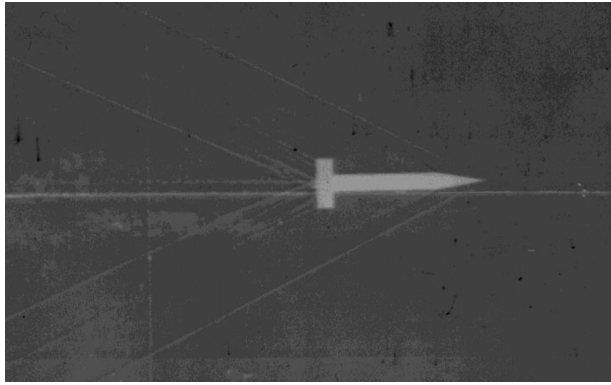


Fig. 14 Example spark range shadowgraph from active microspoiler flight experiment

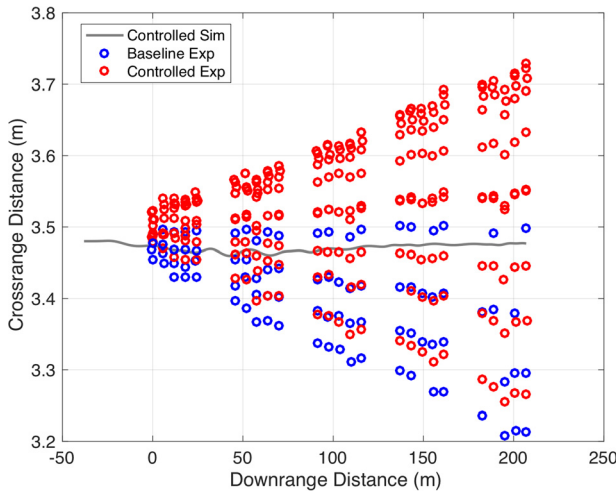


Fig. 15 Cross-range measurements from spark range experiments

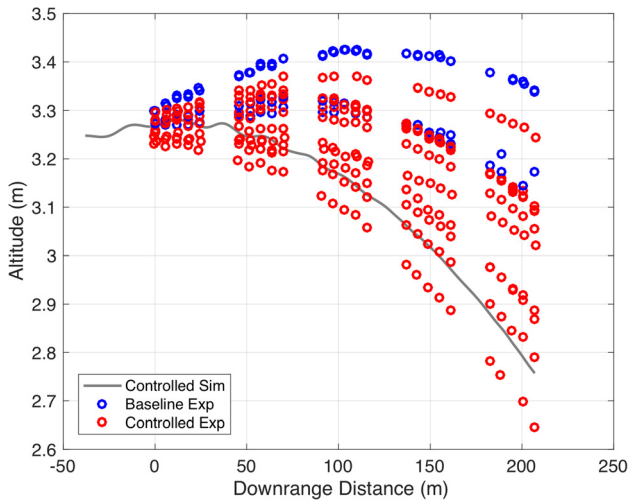


Fig. 16 Altitude measurements from spark range experiments

microspoilers. While the simulated trajectory shows some deviation from the measured values, it matches the data qualitatively and again some of this discrepancy may be caused by perturbations at launch or sabot separation.

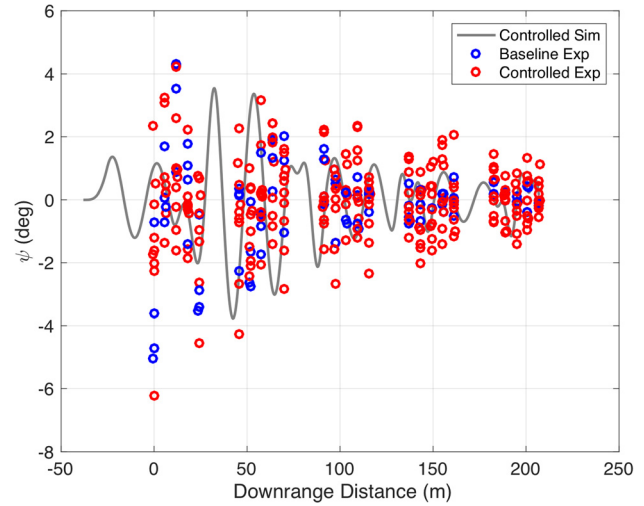


Fig. 17 Yaw angle measurements from spark range experiments

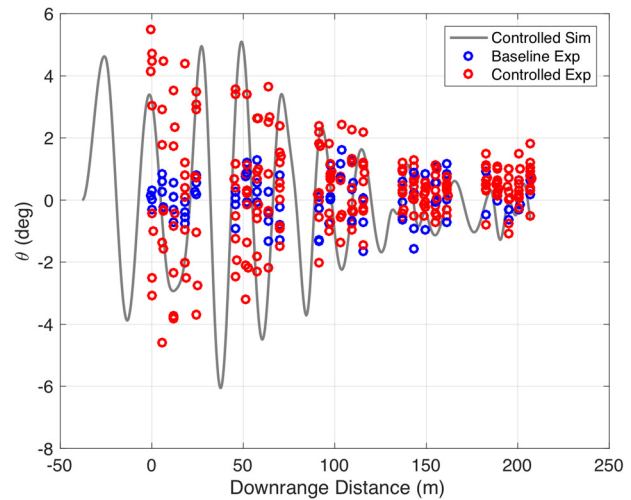


Fig. 18 Pitch angle measurements from spark range experiments

Figures 17 and 18 show the experimentally measured pitch and yaw angles. Figure 17 shows that the yaw angular motion exhibited by both the baseline and controlled rounds is rather high, and there is no clear difference between the two configurations during the first half of the trajectory. These initial yaw perturbations, which are present in both the baseline and controlled rounds, may be due to perturbations caused by sabot separation. However, as the simulation results show, at least some angular motion in the controlled cases is due to the microspoiler mechanism, especially since the measured values are consistently higher in the controlled cases during the second half of the trajectories (greater than about 100 m downrange). Overall, agreement with simulation predictions is quite good as the overall magnitude and decay rate of the yaw angle shows similar trends between simulation and experiment.

In contrast to the yaw angle measurements, the pitch angle data in Fig. 18 shows a clear difference between baseline and controlled trajectories. For the baseline configurations, the measured pitch angle never exceeds 2 deg throughout the trajectory. In contrast, nearly all the controlled configurations exhibited pitch perturbations in excess of 2–3 deg. The pitch angle profiles in Fig. 18 show that the pitching moment perturbations generated by the microspoilers caused significant angular motion early in the trajectory before the projectile spins up. As the projectile spin rate

increases, these pitching moments have less effect as the epicyclic frequency of the projectile increases and its angular momentum grows. These pitch angle responses match those observed in simulation quite well. Note that the likely reason why the baseline and controlled trajectories differ so substantially in pitch but not in yaw is that the projectiles were loaded in a similar roll orientation each time (using a smoothbore barrel). Overall, Fig. 18 is especially important in that it provides evidence that the microspoiler mechanism did indeed activate and demonstrates a strong match between experimental and simulation results.

4 Parameter Estimation

4.1 Aerodynamic Coefficient Estimation. The four baseline projectiles were tested in order to gather aerodynamic data for the basic airframe, which could then be used to extract microspoiler forces and moments from the controlled shots. Given the spark range data, aerodynamic coefficient estimation was performed using the Projectile Aerodynamic Coefficient Estimation (PACE) tool developed by Montalvo and Costello [27] and Gross and Costello [28]. PACE is an advanced parameter estimation tool that compares simulation data from a projectile dynamic model to observed experimental data using the output error method (or maximum likelihood). Using a set of spark range data, the PACE tool runs a projectile simulation and optimizes the underlying aerodynamic parameters until the error between the simulated trajectory and the spark range trajectory is minimized in the least-squares sense. The code uses a so-called meta-optimization routine to choose between a suite of different solvers in order to obtain the globally optimal solution for the aerodynamic parameters [28].

Prior to discussion of parameter estimation results, the aerodynamic expansion employed in PACE must be introduced. The body-frame aerodynamic forces on the projectile, which act at the aerodynamic center of pressure and do not include the contributions of the microspoilers, are given by

$$\begin{Bmatrix} X_A \\ Y_A \\ Z_A \end{Bmatrix} = \frac{\pi}{8} \rho V^2 D^2 \begin{Bmatrix} C_{X0} + C_{X2}(v^2 + w^2)/V^2 \\ C_{Y0} + C_{Nz}v/V \\ C_{Z0} + C_{Nz}w/V \end{Bmatrix} \quad (4)$$

where X_A , Y_A , Z_A represent body-frame components. Note that Eq. (4) assumes that the projectile is symmetric about its spin axis (except for the microspoilers). Also note that this aerodynamic model uses a small angle approximation in calculation of the projectile sideslip and angle of attack.

The steady aerodynamic moment is computed as the cross-product between the distance vector from the center of mass to the center of pressure and the aerodynamic force vector given in Eq. (4). An additional pitching moment coefficient due to angle of attack is also used in the steady moment computation given by

$$C_{m\alpha} = \frac{1}{D} C_{Nz}(x_{COP} - x_{CG}) \quad (5)$$

where x_{COP} is the stationline location of the center of pressure and x_{CG} is the stationline location of the mass center. Finally, the unsteady aerodynamic moment is given as

$$\begin{Bmatrix} L_{UA} \\ M_{UA} \\ N_{UA} \end{Bmatrix} = \frac{\pi}{8} \rho V^2 D^3 \begin{Bmatrix} C_{l0} + \frac{DC_{lp}}{2V} p \\ C_{m0} + \frac{DC_{mq}}{2V} q \\ C_{n0} + \frac{DC_{mq}}{2V} r \end{Bmatrix} \quad (6)$$

In this expression, C_{lp} and C_{mq} represent damping terms while C_{l0} is the roll moment coefficient due to fin cant. Note that, in application of this aerodynamic model in a dynamic simulation, the microspoiler force and moment contributions in Eqs. (1) and (3)

are added to the baseline aerodynamic forces and moments in Eqs. (4)–(6).

To initiate the parameter estimation process, PACE was exercised on flight data from the four baseline shots. The purpose of this was to estimate C_{X0} , C_{l0} , C_{lp} , $C_{m\alpha}$, and C_{mq} of the baseline projectile. Note that because each of the baseline shots exhibited very low angle of attack, C_{X2} and C_{Nz} proved difficult to identify (these usually require use of a yaw inducer in spark range tests, which was not employed here). However, given that the aerodynamics of the Army-Navy Finner have been well characterized previously, estimates of C_{X2} and C_{Nz} from the PRODAS aeroprediction tool [29] were used in lieu of identified experimental data. Also, the trim force coefficients C_{Y0} and C_{Z0} and trim moment coefficients C_{m0} and C_{n0} for the bare airframe were not estimated in either the baseline or active microspoiler configurations. While these coefficients for the bare airframe are ideally zero, in free-flight experiments at least some trim force and moment are usually present. In the baseline flight experiments, these coefficients were not estimated since they usually vary from round to round and would not provide useful information on the nominal bare airframe for the active experiments. Following estimation of the baseline airframe coefficients, PACE was exercised on the active microspoiler flights. In this round of parameter estimation, the body aerodynamic coefficients were fixed and the microspoiler force and moment perturbations (δ_A , δ_{Nz} , and δ_M) were estimated instead. These estimates were then compared to those generated from CFD in Ref. [15].

Several issues were encountered during estimation of the microspoiler forces and moments that were a result of the selected flight test methodology. First, no data was collected regarding the experimentally achieved actuation profile—when the spoilers were actually deployed and when they were retracted. This would have necessitated use of a telemetry system, which would have increased the cost and complexity of the tests considerably. Instead, the actuation profile was parameterized in terms of a frequency, phase, and rise time, and these three parameters were estimated for each trajectory. This parameterization likely introduced some error into the estimation process as the exact actuation profile was unknown. The second issue was that the angular motion induced by the microspoilers dissipated after the projectile spun up (after about the first 100 m of flight as seen in Fig. 18) due to the fact that the spoilers were actuated off of the projectile spin rate. While this was necessary in order to ensure that the projectile did not deviate out of the test range, it meant that spark range data past the first ~100 m of flight were not particularly useful for parameter estimation purposes. In fact, most of the information relevant to microspoiler effectiveness is generated in the first 50–75 m of flight, meaning that only a small subset of the spark range data provided useful information on microspoiler forces and moments. Finally, the presence of possible trim forces and moments in the bare airframe on the active microspoiler shots produced a possible observability issue with respect to the microspoiler forces and moments. Since the effects of trim forces and moments and microspoiler forces and moments on the flight behavior are largely the same, it is difficult to estimate these effects separately. Thus, trim coefficients were not estimated, and the effect of any trim force or moment is absorbed into the microspoiler force and moment coefficient during the estimation process. This likely led to increased round-to-round variability in the estimated microspoiler aerodynamic effects.

To mitigate these issues, several minor adjustments were made to the traditional parameter estimation approach employed in PACE. First, instead of estimating initial conditions from the first spark station, the initial conditions from the gun were estimated instead. Second, the initial condition on pitch rate q was limited within the range of -2.5 rad/s to 2.5 rad/s. This limit was enforced because the effect of the pitching moment caused by the microspoilers was found to be very similar to the effect caused by an initial pitch rate, meaning these parameters were largely unobservable with respect to one another. Thus, initial estimated q was

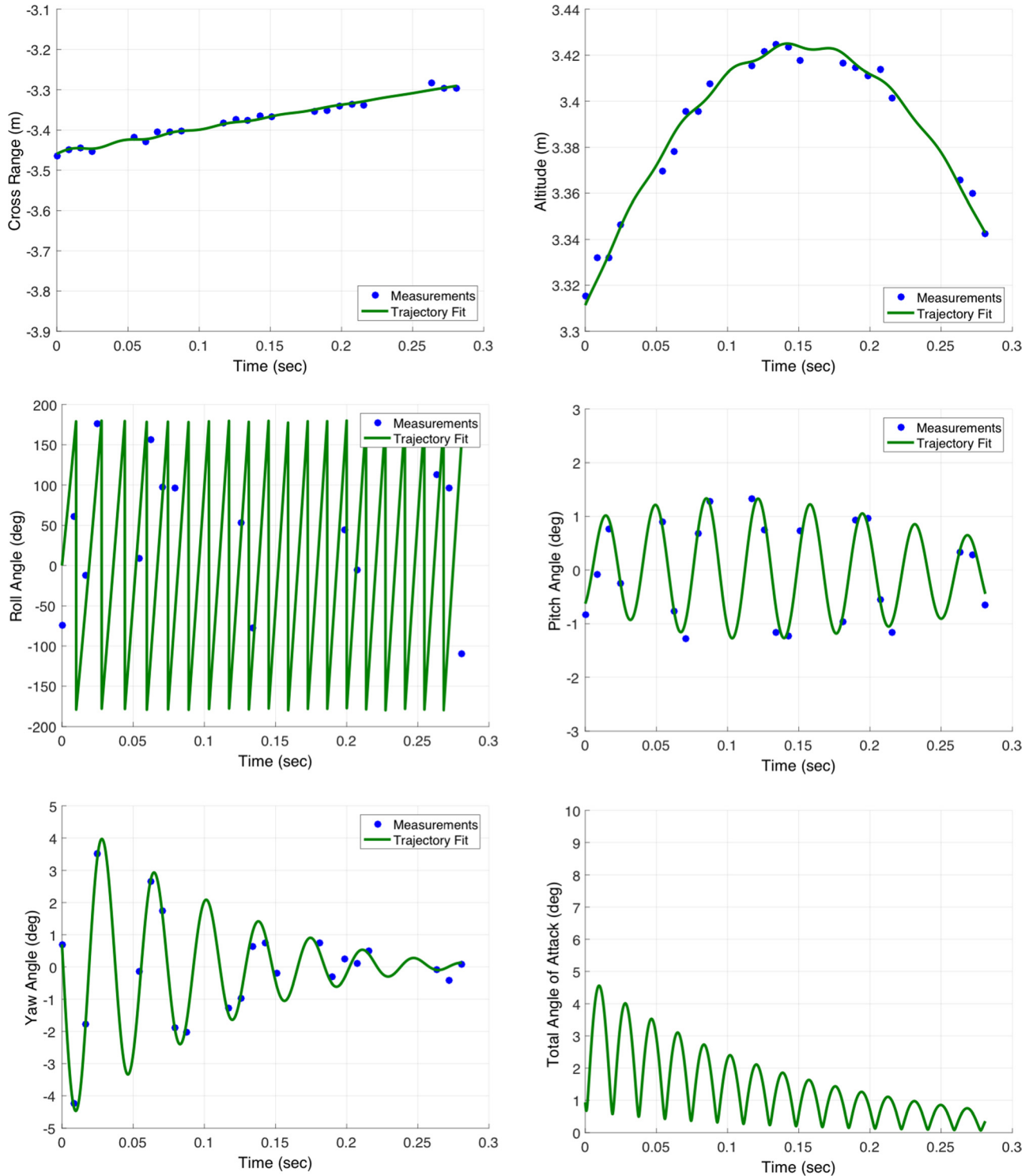


Fig. 19 Example baseline no-microspoiler trajectory fit

limited to ± 2.5 rad/s, as this was the maximum value observed in the baseline no-microspoiler shots. Finally, only a subset of active microspoiler trajectories (four out of ten) was used in the final parameter estimation process. These trajectories were selected because they provided clean and accurate fits in spite of the aforementioned issues with data quality, completeness, and the possible presence of trim aerodynamics.

Figure 19 shows example results for one baseline projectile trajectory fit. This includes time histories of cross-range, altitude, roll, pitch, yaw, and angle of attack. Note that for all other

Table 3 Estimated aerodynamic coefficients for baseline no-microspoiler experiments

	Estimated ($M = 2.0$)	Estimated ($M = 2.5$)
C_{x0}	0.54	0.46
C_{f0}	0.18	0.10
C_{lp}	-17.3	-13.1
C_{mz}	-23.8	-14.4
C_{mq}	-402.2	-361.6

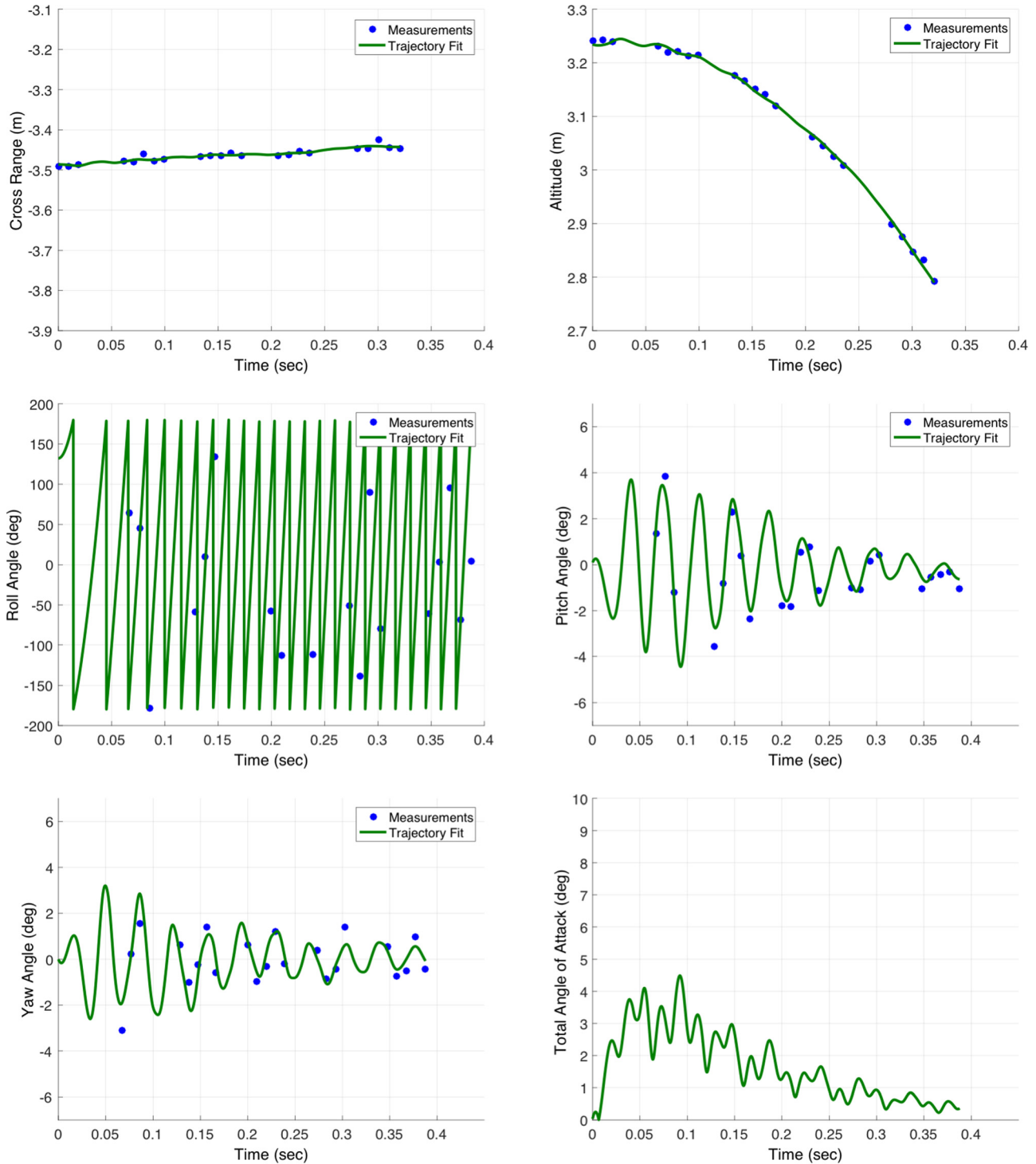


Fig. 20 Example controlled projectile trajectory fit

Table 4 Estimated aerodynamic coefficients for active microspoiler flight experiments

Serial number	Estimated launch Mach number	Axial drag (δ_A), N	Normal force (δ_{NZ}), N	Moment (δ_M), N·m
39668	1.95	-48.5	72.1	6.27
39671	2.06	-49.7	88.2	7.00
39675	1.98	-42.0	29.0	4.45
39676	1.83	-42.0	57.2	8.78
Average	—	-45.5	61.6	6.62
CFD prediction (Mach 2.0)	—	-18.5	47.8	5.92

baseline flight experiments, the trajectory fits were quite satisfactory, similar to that shown in Fig. 19. Table 3 lists the aerodynamic parameters C_{X0} , C_{l0} , C_{lp} , C_{mz} , and C_{mq} estimated from these data. Note that the estimated pitching moment coefficients C_{mz} and C_{mq} were within several percent of those predicted from PRODAS. The drag coefficient C_{X0} exhibits about 10% error with respect to the PRODAS prediction. However, the estimated C_{X0} value at Mach 2.5 in Table 2 shows very good agreement with the CFD predictions reported in Refs. [30] ($C_{X0} \approx 0.47$) and [14] ($C_{X0} \approx 0.45$). Given this close agreement with the results of two independent prior studies, it is likely that the semi-empirical PRODAS prediction of C_{X0} is in error by about 10% and the estimated value in Table 3 is very close to the true value.

A final note is in order regarding the roll measurement data presented in Fig. 19. The 30 mm-diameter projectile used in the flight experiments described here is somewhat small relative to the size of the shadowgraph generated in the TEF. As a result, the roll pin installed on the base of the round is also quite small and may be difficult to identify. In many shadowgraphs, it proved impossible to clearly identify the location of the roll pin, especially in the presence of the shocks and aerodynamic features in the wake of the projectile. Furthermore, in some pitch and yaw orientations, the roll pin may be shadowed by the aft body fins, again precluding a roll angle measurement. For these reasons, the number of roll angle measurement points in the data presented in Fig. 19 is less than the number of pitch or yaw angle measurements. The same is true for the data in Fig. 20.

Figure 20 shows a trajectory fit for an example spark range flight experiment with the controlled projectile. The fits were obtained in PACE by using the estimated baseline ANF aerodynamic parameters in Table 3 and optimizing the microspoiler force and moment values to match the spark range data. A total of four trajectories were selected for use in fitting based on the quality of the data. In addition to the microspoiler force and moment values, the projectile initial ϕ , v , w , q , and r were estimated, as well as the microspoiler oscillation frequency, phase, and rise time constant. Interestingly, the average estimated microspoiler actuation frequency was 64.4 Hz, which was very close to the target rate of 70 Hz. The estimated microspoiler forces and moments from these fitting experiments are shown in Table 4, as are the estimated launch Mach number and the estimated force and moment values averaged over the four experiments. Figures 21 and 22 show these experimentally derived estimates of δ_M , δ_{NZ} , and δ_A overlaid with the predicted CFD values.

The estimated microspoiler forces and moments in Table 4 exhibit several interesting trends. First, the moment values estimated from the flight data match the CFD predictions within about 10% at Mach 2.0, which is judged to be very favorable

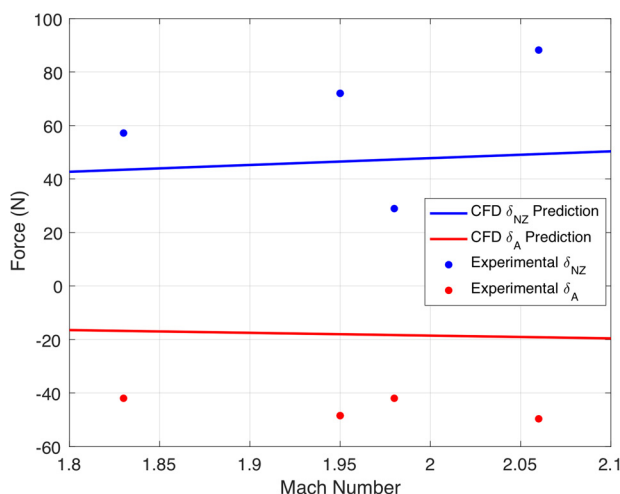


Fig. 21 Microspoiler perturbation forces versus Mach number

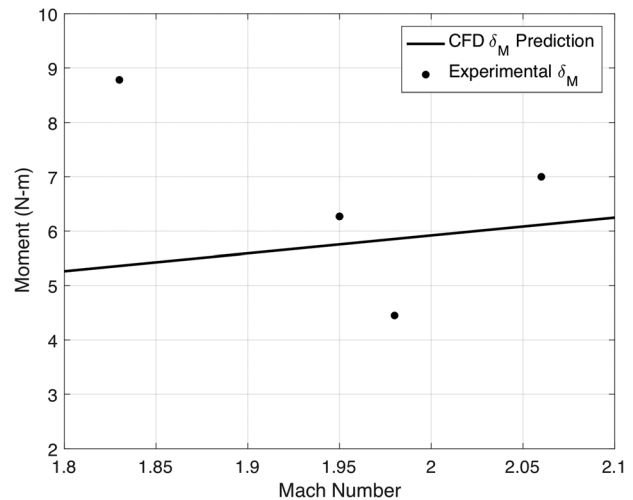


Fig. 22 Microspoiler perturbation moments versus Mach number

agreement. Because the perturbation moment is the main driver behind control authority for this mechanism, this experimental validation provides significant confidence that the maneuver authority predicted from CFD is physically realizable, at least in this speed range. Variation in the moment coefficient in Table 4 is likely due to the presence of bare airframe trim moments, which as mentioned previously are not being estimated separately. The estimated perturbation forces δ_A and δ_{NZ} exhibited higher error compared to the CFD predictions. There are several possible causes for this. First, the perturbation normal force δ_{NZ} is only mildly observable from the spark range data, as it has less impact on the angle of attack response compared to the moment δ_M . This poor observability means that the estimated values may be subject to more error. Note that the normal force estimates showed a much larger variation between flights (from 29.0 N to 88.2 N) compared to δ_A . This is in part because of poor observability but is also likely to be due to the presence of trim forces which vary on a round-to-round basis due to manufacturing tolerances and slight mass asymmetries. In contrast, the δ_A estimates exhibited much less variation but were consistently higher (or more negative) than the CFD predictions. This is likely caused by the fact that the baseline ANF drag coefficient C_{X0} in Table 3 was estimated to be lower than that of the PRODAS ANF by about 10%. Interestingly, when the same fitting process was performed for the active flight experiments using the C_{X0} value from PRODAS, the estimated microspoiler δ_A coefficients nearly matched those predicted in CFD. However, because the experimentally estimated data in Table 3 is corroborated by Scheuermann et al. [14] and Bhagwandin [30], the value for C_{X0} in Table 3 is probably close to the correct value. Thus, it is likely that the experimentally estimated δ_A forces in Table 4 are correct and the microspoilers do, in fact, exhibit higher drag than that predicted in CFD.

4.2 Simulation Results Using Identified Aerodynamics. To quantify control authority with the experimentally estimated microspoiler forces and moments, a series of trajectory simulations was performed. The ANF projectile was simulated over 1 km using the inertial parameters of the projectile employed in experimental tests. The projectile was launched at Mach 2.0 with an initial roll rate of 72 Hz, which is approximately the steady-state roll rate at this muzzle velocity with a fin cant of 1.25 deg. Four sets of microspoilers were used (one between each set of fins), each with a 90 deg activation window [13]. The spoilers were oscillated at the projectile roll frequency, and maximum control authority was commanded in the negative cross-range

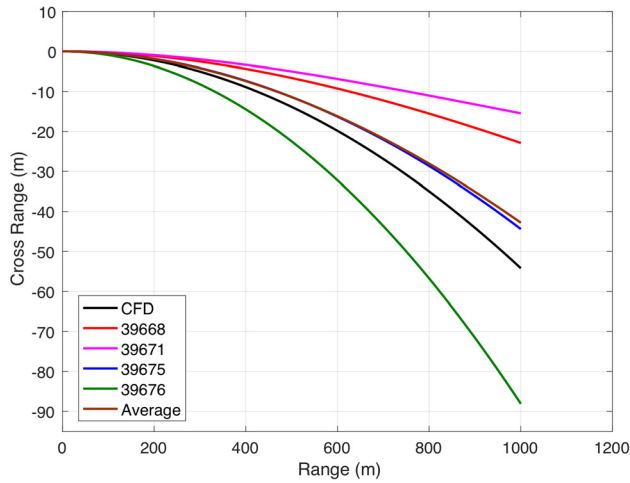


Fig. 23 Cross-range versus range for control authority simulations

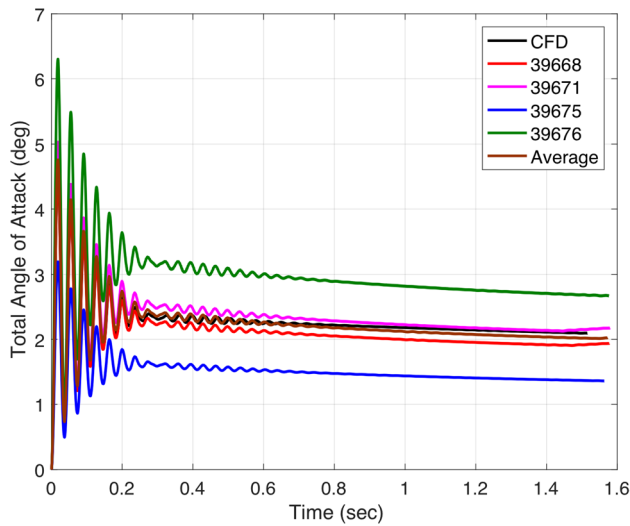


Fig. 24 Angle of attack versus time for control authority simulations

direction. Because experimental data are only available around Mach 2.0, the drag coefficients C_{X0} and C_{X2} were set to zero, leaving only the microspoiler contribution to drag. Thus, the projectile velocity did not drop below about Mach 1.8 over the 1 km flight. This was done so that control authority could be studied using the experimentally identified force and moment values near the Mach range at which they are valid. A total of six simulations were performed, each corresponding to an estimated force and moment value listed in Table 4.

Figures 23 and 24 show the results of these simulations. The cross-range results in Fig. 23 show that control authority estimates vary noticeably using the experimental data, but the control authority for the trajectory using the average experimental force

and moment estimates in Table 4 is similar to that predicted with the CFD values (within 20%). Figure 24, showing angle of attack time histories for each simulation, shows that the trim angle of attack induced by the microspoilers is a function of the spoiler moment only, not the normal force, since the normal force acts at the projectile mass center and does not directly induce angular motion. For instance, trajectory 39675 has the lowest trim angle of attack because it has the lowest predicted δ_M , but it exhibits moderate control authority because its predicted δ_{NZ} is also relatively low. Note that because the mechanism is located at the rear of the projectile, the spoiler normal force and pitching moment perturbations actually induce control in opposite directions. As a result, a high δ_M and low δ_{NZ} will result in maximum control authority. Accordingly, trajectory 39676, which has a large δ_M but only a moderate δ_{NZ} value, shows the greatest control authority and angle of attack.

It is interesting to compare the trajectory prediction results in Figs. 23 and 24 and the experimentally derived forces and moments in Table 4 with previous experimental results, particularly those described in Ref. [18]. Massey and Silton [18] describe spark range flight experiments with a pin-fin mechanism that deploys out of the body and remains statically deployed during flight. The pins used in Ref. [18] are similar in nature to the microspoilers employed here, except that there are two pins instead of eight and the pins are generally larger than the microspoilers. The tests in Ref. [18] were conducted with minimal roll rate so that divert distance could be measured downrange. Due to the higher muzzle velocity, the projectile used in Ref. [18] had a somewhat different aerobody shape than that employed here. These discrepancies in the system and test conditions mean that the results should not be expected to match precisely, but a comparison may still be informative.

Table 5 shows a summary of the results from Ref. [18] compared against those observed here, where the microspoiler normal force is taken from Table 4 and the lateral acceleration is derived from Fig. 23. The observed normal force in the current experiments was somewhat less on average compared to that in Ref. [18], which is to be expected considering the much lower muzzle velocity. In fact, this reduction in normal force is less than would be expected, given the large discrepancy in dynamic pressure and the fact that the microspoilers in the current flight experiment oscillate into and out of the body. This is likely because the arrangement and number of spoilers are highly optimized in this work compared to Ref. [18]. The observed lateral acceleration in the current experiments is noticeably lower than in Ref. [18]. This is again likely due to the significantly lower muzzle velocity at which these tests were performed. Note that Ref. [15] predicts that lateral acceleration capability scales exponentially with Mach number for this type of mechanism, which is corroborated by the acceleration results in Table 5. Taken as a whole, the observations in Ref. [18] show similar trends to the results provided here, reinforcing the conclusions of Ref. [18] that the microspoiler actuators generate quite large control forces considering their small size.

Overall, the results presented here demonstrate that the microspoiler mechanism seems to maintain its control effectiveness while undergoing dynamic oscillation at typical fin-stabilized projectile spin rates. Control authority estimates using experimentally derived data, while showing significant variation, generally show favorable agreement with CFD predictions and provide further evidence of the effectiveness of the mechanism as a control actuator for fin-stabilized projectiles.

Table 5 Comparison of results with experiments in Ref. [18]

	Launch velocity (Mach)	Static margin (calibers)	Number of actuators	Observed normal force (N)	Observed lateral acceleration (g's)
Microspoiler experiments (this work)	1.95 (avg.)	1.0	8	62 (avg.), 29–88 (range)	3.4 (avg.), 1.2–7.1 (range)
Pin fins in Ref. [18]	4.26	1.5	2	80	14

5 Conclusion

A novel rotary mechanism for smart weapons control actuation has been proposed. The actuator provides unique benefits in terms of shock survivability, compactness, and mechanical simplicity, and offers actuation bandwidths suitable for the majority of fin-stabilized projectiles. Through use of a suitable motor offering faster rotation rates, the design can also be adapted for use on spin-stabilized projectiles as well. Integrated test projectiles were constructed in which the rotary actuator is used to drive a set of microspoilers between one set of aft fins. Flight experiments in which the microspoilers oscillated near the projectile roll frequency verified shock survivability of the actuator and provided flight data for system identification. A parameter estimation process yielded microspoiler force and moment perturbation values that compare favorably with prior CFD predictions. These parameter estimates verify that the microspoiler mechanism maintains control effectiveness when actuated in an oscillatory fashion at the projectile roll rate. Overall, the experimentally derived aerodynamic estimates reported here will prove useful in the design of future smart weapons concepts that leverage microspoilers for active control.

Acknowledgment

This work was sponsored by the Defense Advanced Research Projects Agency, Tactical Technology Office, under Contract No. HR0011-14-C-0126. The views, opinions, and/or findings expressed are those of the authors and should not be interpreted as reflecting the official views or policies of the Department of Defense or the U.S. Government.

Nomenclature

C_i	= various projectile aerodynamic coefficients
D	= projectile reference diameter
$\mathbf{I}_B, \mathbf{J}_B, \mathbf{K}_B$	= projectile body frame unit vectors
L_{MS}, M_{MS}, N_{MS}	= body-frame components of microspoiler moment
L_{UA}, M_{UA}, N_{UA}	= body-frame components of unsteady aerodynamic moment
M	= Mach number
p, q, r	= body-frame components of the projectile angular velocity
s	= nondimensional spoiler extension distance
u, v, w	= body-frame components of the projectile mass center velocity
V	= total velocity of projectile mass center
X_A, Y_A, Z_A	= body-frame components of aerodynamic forces
X_{MS}, Y_{MS}, Z_{MS}	= body-frame components of microspoiler forces
$\delta_A, \delta_{NY}, \delta_{NZ}$	= microspoiler perturbation axial force, y-axis normal force, z-axis normal force
$\delta_L, \delta_M, \delta_N$	= microspoiler perturbation roll moment, pitch moment, yaw moment
ρ	= air density
ϕ, θ, ψ	= projectile Euler rotation angles

References

- [1] Siouris, G. M., 2004, *Missile Guidance and Control Systems*, Springer, New York, p. 3.

- [2] Costello, M., 1997, "Range Optimization of a Fin-Stabilized Projectile," *AIAA Paper No. 97-3724*.
- [3] Ollerenshaw, D., and Costello, M., 2008, "Model Predictive Control of a Direct Fire Projectile Equipped With Canards," *ASME J. Dyn. Syst. Meas. Control*, **130**(6), p. 061010.
- [4] Chandgadkar, S., and Costello, M., 2002, "Performance of a Smart Direct Fire Projectile Using a Ram Air Control Mechanism," *ASME J. Dyn. Syst. Meas. Control*, **124**(4), pp. 606–612.
- [5] Baines, W. R., and Sumrall, C. W., 1985, "Ram Air Steering System for a Guided Missile," U.S. Patent No. **US 4522357 A**.
- [6] Costello, M., and Agarwalla, R., 2000, "Improved Dispersion of a Fin-Stabilized Projectile Using a Passive Moveable Nose," *AIAA Paper No. 2000-4197*.
- [7] Landers, M., Hall, L., Auman, L., and Vaughn, M., Jr., 2003, "Deflectable Nose and Canard Controls for a Fin-Stabilized Projectile at Supersonic and Hypersonic Speeds," *AIAA Paper No. 2003-3805*.
- [8] Kennedy, W. B., and Mikkelsen, C., 1998, "AIT Real Gas Divert Jet Interactions: Summary of Technology," *AIAA Paper No. 98-5188*.
- [9] Tournes, C., Shtessel, Y., and Shkolnikov, I., 2006, "Missile Controlled by Lift and Divert Thrusters Using Nonlinear Dynamic Sliding Manifolds," *J. Guid. Control Dyn.*, **29**(3), pp. 617–625.
- [10] Frost, G., and Costello, M., 2004, "Linear Theory of a Projectile With a Rotating Internal Part in Atmospheric Flight," *J. Guid. Control Dyn.*, **27**(5), pp. 898–906.
- [11] Frost, G., and Costello, M., 2006, "Control Authority of a Projectile Equipped With an Internal Unbalanced Part," *ASME J. Dyn. Syst. Meas. Control*, **128**(4), pp. 1005–1012.
- [12] Rogers, J., and Costello, M., 2008, "Control Authority of a Projectile Equipped With a Controllable Internal Translating Mass," *J. Guid. Control Dyn.*, **31**(5), pp. 1323–1333.
- [13] Dykes, J., Montalvo, C., Costello, M., and Sahu, J., 2012, "Use of Microspoilers for Control of Finned Projectiles," *J. Spacecr. Rockets*, **49**(6), pp. 1131–1140.
- [14] Scheuermann, E., Costello, M., Silton, S., and Sahu, J., 2015, "Aerodynamic Characterization of a Microspoiler System for Supersonic Finned Projectiles," *J. Spacecr. Rockets*, **52**(1), pp. 253–263.
- [15] Leonard, A., Rogers, J., and Jubaraj, S., 2016, "Aerodynamic Optimization of Microspoiler Mechanisms for Projectile Flight Control," *J. Spacecr. Rockets*, (accepted).
- [16] Massey, K., McMichael, J., Warnock, T., and Hay, F., 2008, "Mechanical Actuators for Guidance of a Supersonic Projectile," *J. Spacecr. Rockets*, **45**(4), pp. 802–812.
- [17] Massey, K. C., and Guthrie, K. B., 2005, "Optimized Guidance of a Supersonic Projectile Using Pin Based Actuators," *AIAA Paper No. 2005-4966*.
- [18] Massey, K. C., and Silton, S. I., 2006, "Testing the Maneuvering Performance of a Mach 4 Projectile," *AIAA Paper No. 2006-3649*.
- [19] Celmins, I., 2007, "Design and Evaluation of an Electromechanical Actuator for Projectile Guidance," U.S. Army Research Laboratory, Aberdeen, MD, Technical Report No. **ARL-MR-0672**.
- [20] Fresconi, F., Celmins, I., and Fairfax, L., 2011, "Optimal Parameters for Maneuverability of Affordable Precision Munitions," U.S. Army Research Laboratory, Aberdeen, MD, Technical Report No. **ARL-TR-5647**.
- [21] Kang, C.-G., Lee, J.-S., and Han, J.-H., 2014, "Development of Bi-Stable and Millimeter-Scale Displacement Actuator Using Snap-Through Effect for Reciprocating Control Fins," *Aerosp. Sci. Technol.*, **32**(1), pp. 131–141.
- [22] Celmins, I., Fresconi, F., and Nelson, B., 2014, "Actuator Characterization of a Man-Portable Precision Maneuver Concept," *Def. Technol.*, **10**(2), pp. 141–148.
- [23] Costello, M., and Rogers, J., 2011, "BOOM: A Computer-Aided Engineering Tool for Exterior Ballistics of Smart Projectiles," U.S. Army Research Laboratory, Aberdeen, MD, Technical Report No. **ARL-CR-670**.
- [24] Reuleaux, F., 1876, *Kinematics of Machinery: Outlines of a Theory of Machines* (Translated by A. B. W. Kennedy), MacMillan and Company, London, p. 116.
- [25] Dueck, R., and Reid, K., 2012, *Digital Electronics*, Cengage Learning, Boston, MA, p. 286.
- [26] Bukowski, E., 2009, "Evaluation of Commercial-Off-the-Shelf Lithium Batteries for Use in Ballistic Telemetry Systems," U.S. Army Research Laboratory, Aberdeen Proving Ground, Aberdeen, MD, Technical Report No. **ARL-TR-4840**.
- [27] Montalvo, C., and Costello, M., 2010, "Estimation of Projectile Aerodynamic Coefficients Using Coupled CFD/RBD Simulation Results," *AIAA Paper No. 2010-8249*.
- [28] Gross, M., and Costello, C., 2016, "Projectile Parameter Estimation Using Meta-Optimization," *AIAA Paper No. 2016-0538*.
- [29] Arrow Tech, 2000, "PRODAS Version 3 Documentation," Arrow Tech Associates, Burlington, VT.
- [30] Bhagwandin, V., 2016, "High-Alpha Prediction of Roll Damping and Magnus Stability Coefficients for Finned Projectiles," *J. Spacecr. Rockets*, **53**(4), pp. 720–729.